Lawrence Berkeley National Laboratory
LBL Publications

Title

A Transmission Electron Microscope Study of Deep-Sea Manganese Nodules

Permalink

https://escholarship.org/uc/item/3g87f3fw

Authors

von Heimendahl, M
Hubred, Gale L
Fuerstenau, D W
et al.

Publication Date

1975

Copyright Information

A TRANSMISSION ELECTRON MICROSCOPE STUDY OF DEEP-SEA MANGANESE NODULES

M. von Heimendahl, Gale L. Hubred, D. W. Fuerstenau,
and Gareth Thomas

January, 1975

DISCLAIMER

A TRANSMISSION ELECTRON MICROSCOPE STUDY OF DEEP-SEA MANGANESE NODULES

by

M. von Heimendahl[*], Gale L. Hubred,
D. W. Fuerstenau and Gareth Thomas
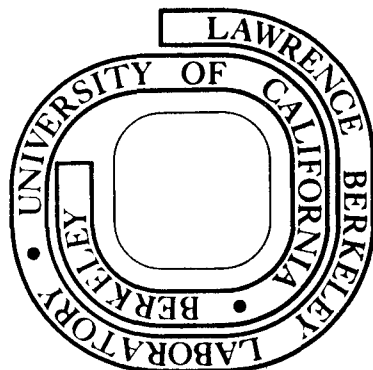
Department of Materials Science and Engineering
University of California, Berkeley, California 94720

ABSTRACT

Two Pacific Ocean manganese nodules, one from the ocean basin and one from a sea-mount, were examined in transmission electron microscopes at 100kV and 650 kV. Of the many specimens examined, ten electron diffraction crystal spot patterns were identified. Sodium birnessite was observed six times and todorokite, Giavanoli's synthetic birnessite, hydrohausmanite and $\gamma-Fe_2O_3$ were each found one time. Ferric hydroxide was synthesized in the laboratory and shown to be the same as the primary iron mineral observed in the manganese nodules. The ferric hydroxide was found to range in particle size from 30 to 450 Å. Manganese oxide particles were frequently found embedded in a mass of smaller ferric hydroxide particles.

[*]Work done while on sabbatical leave from the Institut für
Werkstoffwissenschaften I, der Universität Erlangen-Nürnberg, Germany.

INTRODUCTION

Manganese nodules are mineral concretions found on all of the ocean floors. The amount of the Pacific Ocean surface deposit alone has been estimated to be greater than 10^{11} tons (Mero, 1965, Zenkevitch and Skoryakova, 1961). Nodules are comprised of manganese and iron oxides and hydroxides together with varying amounts of aluminum silicate and other minerals. Nodules are of potential economic interest because of the significant amounts of such valuable metals as nickel, copper, and cobalt contained within them. The nature and occurrence of nodules have been discussed in detail elsewhere by Mero (1965), Tooms et al. (1969) and extensive bibliographies are available (Glasby, 1972, 1973; Glasby and Hubred, 1973). The specific surface area of nodules is approximately 200 square meters per gram (Fuerstenau et al., 1973), indicating that the minerals constituting nodules are of extremely fine crystallite size. Although deep-sea nodules have been the subject of many papers, there is still considerable disagreement about their mineralogy. The complex natural assemblage of particles smaller than one micron found in manganese nodules is ideally suited to study by transmission electron microscopy. The purpose of this work is to initiate such a study of manganese nodule mineralogy. The procedures utilized in this transmission electron microscopic study are complex, but it is hoped that the investigation may shed further light on the complex mineralogy of manganese nodules.

BACKGROUND LITERATURE

Buser and Grütter (1956) first identified the layered manganese oxides in nodules and they called them 7 Å and 10 Å manganites because of the basal spacings of the layers. Most authors, Tooms et al. (1969), Han

(1971), accept the identity of 10 Å manganite with todorokite. However, Giovanoli et al. (1973; 1971; 1970 a,b; 1969 a,b; 1968; 1967) have con-, ducted an extensive survey of the manganese oxides and concluded that what is commonly identified as todorokite is a complex mixture of altera- tion products of "buserite" dehydrating to birnessite. "Buserite" is the newly proposed name for the 10 Å manganite which had originally been prepared by Buser and Grütter (1956) and also observed by them in manganese nodules. Giovanoli (1973) has prepared todorokite containing up to a few percent of various metal cations.

The relationship between $\delta-MnO_2$, birnessite, and 7 Å manganite is more complex. Some authors, McMurdie (1944), Glemser et al. (1961), Burns and Fuerstenau (1966), have considered $\delta-MnO_2$ as a distinct mineral. Several authors, Tooms et al. (1969) and Han (1971), have agreed upon the identity of birnessite with the 7 Å manganite originally synthesized and found in manganese nodules by Buser and Grütter (1956). Bricker (1965) showed that $\delta-MnO_2$ is identical with birnessite except that it lacks the basal plane reflections in diffraction work because of its small particle size. Giovanoli (1969) has concluded that $\delta-MnO_2$ is a family of oxides with a continuous series of lattice parameter alterations resulting from the substitution of various cations between the oxide layers. He has proposed two new ASTM file cards for the minerals "synthetic birnessite" (sodium free) and "sodium birnessite", both primary members of the $\delta-MnO_2$ series. In the text of this paper we shall use the terminology s-birnessite to represent the so-called synthetic birnessite of Giovanoli since the minerals examined in the nodules are not synthetic. Table I has been provided to summarize the interrelationships between the several manga- nese oxides discussed above. Other minerals claimed to have been found

in manganese nodules include psilomelane, vernadite, woodruffite, pyro-
lusite, γ-MnO_2, and cryptomelane (Andrushchenko and Skornyakova, 1969);
Gattow and Glemser, 1961).

The dehydration of todorokite to birnessite has been observed by
several authors, Cronan (1967), Stevenson and Stevenson (1970), and
Giovanoli (1971). Brown (1971) has reversed this transition, hydrating
birnessite back to todorokite by the use of an autoclave. The dehydration
proceeds at an observable rate under laboratory conditions, indicating
the need for an investigation of nodules that have been freshly gathered
and stored in a wet atmosphere.

Iron Compounds

Goethite, FeO(OH) has been the most commonly identified iron phase
found in nodules (Han, 1971; Arrhenius, 1963); but recent Mössbauer
spectra have shown that the iron is nearly all present as ferric hydroxide
gels approximately 100 Å in diameter (Hrynkiewicz et al., 1970; Johnson
and Glasby, 1969). Hrynkiewicz et al. (1970) have shown very clearly
that the surprisingly simple spectrum of manganese nodules is identical
with that of ferric hydroxide. Brown (1971) has found the same spectrum
and also detected a small amount of ferrous iron. The ferrous ion in
nodules may reside in the manganese layered oxides, as may the other
divalent metal cations.

Silicate Compounds

Less attention has been directed toward the silicate phases, but
montmorillonite, phillipsite, and illite have been found in manganese
nodules. The silicate compounds can consume large amounts of acid in

an acid leach system and would therefore be of interest to the extractive metallurgist.

Nickel, Copper and Cobalt in Nodules

The mechanism by which transition metals and trace elements are incorporated into nodules is one of the most poorly understood subjects, and yet these elements are most attractive because of their potential economic value. On the basis of bulk chemical analysis, Goldberg (1954) found that Ni and Cu positively correlate with Mn in nodules and that Co, Ti and Zn increase with the Fe content. Using an electron probe X-ray microanalyzer, Burns and Fuerstenau (1966) demonstrated that there is a distinct correlation between Fe, Co, Ti and Ca and also a pronounced association between Ni, Cu, Zn and Mg, which are enriched in the Mn phase. Willis and Ahrens (1962) found that the Ni and Cu concentration in nodules varies directly with each other.

There are several theories on the manner in which these elements occur in nodules. Goldberg (1954) and Krauskopf (1956) supported the theory that these metal ions have been adsorbed from sea water as counter ions in the electrical double layer at the surface of the negatively charged manganese oxides (scavenging actions). Murray et al. (1968) studied the adsorption of aqueous metal ions on synthetic manganese manganite and found that Ni, Cu and Co exhibit marked specific adsorption in this system. On the other hand, Buser and coworkers (1956, 1954, 1955) believe that these cations substitute for Mn^{+2} in the manganite minerals by an ion exchange mechanism. Burns (1965) suggested the possibility of oxidation of Co^{+2} to Co^{+3} in the sea environment. The reaction is assumed to be catalyzed by $Fe(OH)_3$ and is also favored by $Co(OH)_3$ forming a solid

solution with $Fe(OH)_3$. Arrhenius and Bonatti (1965) suggested that manganese dioxide formed by rapid precipitation under comparatively reducing circumstances may offer a favorable condition for solid solution of Co^{+2}. Burns (1970) postulated that the nickel in $\delta-MnO_2$ in manganese nodules is mostly due to the oxidation of Ni^{+2} to Ni^{+4} on the basis of crystal field theory. From extensive thermodynamic calculations, Han (1971) has shown that the concentrations of ions in sea water are those in equilibrium with their oxides. He has postulated, and demonstrated analytically, that nodules are comprised of flocculated oxide particles. The present investigation has included a search for nickel, copper and cobalt compounds to test these concepts.

It is clear, then, that there remains a need for further characterization of manganese nodules and especially to positively identify the mineral composition. The transmission electron microscope (TEM) is a powerful tool which has not been used, to the knowledge of the authors, to full advantage in the study of deep-sea manganese nodules. Okada and Shima (1969) and Buser and Grütter (1956) published electron microscope pictures of nodules but did not provide crystal diffraction patterns. The complex natural assemblege of particles smaller than 1 micron found in manganese nodules is ideally suited to study by TEM. The purpose of this work is to begin this study.

EXPERIMENTAL METHODS

Sample Description

The average chemical composition and original location of the two different samples of manganese nodules that were studied are shown in Table II.

The samples were chosen to represent a deep-water and a sea-mount environment and have been intensively studied in other respects (Han, 1971). The samples which were drawn from a composite of many nodules for a single station, were ground, sized and stored for several months with access to air.

A nodule powder of size fraction less than 74 microns was prepared in a 3 gram per liter suspension and then subjected to sonic energy for various times with a "SONIC DISMEMBRATOR"[*]. Test runs with different times of ultrasonic treatment between 1 minute and 30 minutes at full power showed no differences in microscopic examination. Therefore, a time of 3 minutes was chosen for subsequent experiments.

Electron Microscopy

One droplet of the suspension was placed on a carbon film supported by a standard 200-mesh grid and allowed to dry in air at room temperature, as described by von Heimendahl (1970). The suspension was applied to the side of the carbon film facing the grid. When applied to the other side, the film would roll up and be destroyed. After 15 to 30 minutes, the water was evaporated and all particles settled on the film.

In the microscope, "d" spacings, corresponding to the Bragg condition for reflecting planes ($2d\sin\theta = \lambda$), can be measured from observed diffraction spots or rings in diffraction patterns by using the camera constant λL. Analysis is carried out as described in several references (e.g., Thomas, 1962; Hirsch et al., 1965; von Heimendahl, 1970). For calibration in electron diffraction work, between one-third and one-half

---

[*]Quigley-Rochester Inc., Rochester, New York 14607.

of the grid area was afterwards evaporated with gold. The camera constant λL (λ = electron wavelength, L = effective camera length) was determined as the mean value from the strong (111)- and (311)-Debye-Scherrer rings of the gold.

The data reported here were obtained with a 100 kV Siemens Elmiskop IA and a 650 kV Hitachi electron microscope. The higher voltage provides greater penetration and is useful for large particles, (e.g., 1μm or more in thickness). In the case of the Elmiskop, a λL-calibration curve vs objective lens current (430 to 480 mA) could be worked out, using a standard setting of 63 mA for the intermediate lens and 208 mA for the projector lens current. Various thicknesses of the samples and use of different sample holders result in different height positions in the microscope. The lower the specimen, the smaller is λL and the larger must be the lens power (current) of the objective lens. Thus, after appropriate calibrations the values of λL can be corrected for such factors. The accuracy in d-value determination gained this way was better than ±0.7 percent for the best spot patterns and better than ±1.2 percent for the remaining cases.

Data Processing

Unfortunately, for many of the minerals which have been reported in manganese nodules or in ASTM file cards, only d-spacings but not structure is given so that such minerals could not be considered in the present work. It should be noted that X-ray analysis of individual particles may not resolve all possible d-values because of intensity factors and preferred orientation. Furthermore, in electron diffraction spot patterns only reflecting planes with zone axes approximately parallel

to the incident electron beam satisfy the Bragg reflecting condition, thus not all possible d spacings can be found for a given particle. Therefore, a computer program was used to compute all of the d values larger than 0.9Å for each mineral for which the lattice parameters were available. The complete set of d values which were computed and indexed were then stored on computer cards in binary code and could be searched for a fit with the d values observed from TEM investigations. Appendix 1 contains a list of the minerals considered. ASTM file and a literature search provided 74 sets of crystal lattice parameters. Thirty-three manganese compounds and eighteen iron compounds were considered. This is not an exhaustive table because the numerous cations and anions available in the ocean might all participate in the mineral formation.

RESULTS AND DISCUSSION

Figures 1 and 2 are typical survey pictures of manganese nodule powders of the two different origins. Figure 1 shows the primary particles of the "deep ocean" nodule 2P-51. One can clearly distinguish two types of particles in these electron micrographs. Type 1 are very thin flakelike particles giving rise to diffraction patterns such as those shown in Figure 3. Type 2 are thick, bulky particles mostly opague to 100 kV electrons but easier to penetrate with the high voltage 650 kV electrons. The diffraction patterns could be identified as montmorillonite (a clay mineral, Appendix 1). This has truly a monoclinic structure (Appendix 1), but may be considered also as pseudohexagonal (Wenk, 1973), the basal plane being identical with the plane of the diffraction pattern and also with the habit plane of the thin clay flakes. From Figures 1 and 2 it may be seen that the nodule 2P-51 contains considerably more

clay than does DWHD-16. To reduce interference from clays in the iden-
tification of other minerals DWHD-16 was more intensively studied than
2P-51.

Figure 2 is from a "sea mount" nodule DWHD-16 and is somewhat different
in appearance although also two populations of particles seem to occur:
small ones about 0.1 to 0.3 μm in size and large ones up to 10 μm in size.
These two types of particles will be referred to as type 3 and type 4,
respectively. It turned out, however, to be difficult, if not impossible,
to identify these particles from their appearance in bright field images
but that detailed and individual particle diffraction analysis would be
necessary. The first observation was that it was usually rather difficult
to obtain crystal spot patterns or even ring patterns. Approximately one-
half hour was spent in obtaining each pattern. This is not surprising in
the light of the difficulty of Okada and Shima (1969), the complexity of
this natural mineral assemblage, and the extremely small particle sizes
involved in many cases. However, the high voltage microscope is advanta-
geous because of its greater penetrating power, and the smaller Bragg angles
provide a wider range of reflections at 650 kV compared to 100 kV. Seven-
teen spot patterns and ten ring patterns were observed. All ring patterns
and ten spot patterns could be identified. (The numerous patterns avail-
able from the clay mineral montmorillonite are not counted in this context.)

The results can be divided into three areas: manganese minerals, iron
minerals, and the interrelationship between the minerals.

Manganese Compounds

Crystal spot patterns for nine manganese oxide particles were obtained
and identified, as discussed previously. Most of the compounds involved,

Appendix 1, are non-cubic and, therefore, they have many d-values, usually several hundred which are larger than 0.9 Å. These are needed in the present case of analysis according to the λL-values of the microscopes used (typically 2 cm-Å). As a consequence of the high "density" of d-values, the rules of vector addition for the reciprocal lattice points can be sometimes satisfied even with incorrect indexing. However, a check of interplanar angles always revealed finally whether the analysis was consistent.

Figures 4 to 8 represent some of the identified manganese compound crystals with their corresponding spot patterns and indexing. In all cases dark field analysis was used to show the crystal from which the pattern originated, but not all those dark field pictures have been provided here. Figures 4 and 8 show examples of such analyses.

In Figure 4 the so-called "rafted fine structure" of the Na-birnessite crystal can be seen. This is probably the same fine structure as observed and discussed earlier by Giovanoli et al. (1970a) in laboratory-produced Na-birnessite. It is interesting that this effect occurs in the manganese nodule, too.

–With regard to Figure 7, it may be remarked that the very thin transparent hexagonal platelet, originating the "star-like" diffraction pattern with its 60-degree symmetry, settled during the preparation technique down parallel to the supporting C-film. So did probably many others of that type (and also the clay minerals described, compare Figure 3). In Figure 7 only the planes parallel to the hexagonal c-axis contribute to the pattern.

The pattern of Figure 7 can be indexed according to the structure of s-birnessite (Table I), in this case the observed d-values of 2.48Å

and 1.43Å respectively for the reflections (10$\bar{1}$0) and (11$\bar{2}$0) are only

0.8 percent larger than the theoretical d-values. Alternatively, it

could be indexed according to the hexagonal structure of Mn (II)-

manganite (IV) in Table I, but in the latter case the agreement with the

theoretical d values was 1.5 percent too small. Thus, it was concluded

that s-birnessite was the more probable structure.

The results of the solved Mn-compound crystal patterns are summarized

in Table III; Appendix 2 provides a list of the unsolved diffraction

patterns. The angle given is the one between the two shortest vectors

from the origin and the lowest order spots, these vectors corresponding

to the two largest d-values. These three parameters determine the whole

pattern. The observed d-values were within 1 percent in agreement with

the theoretical values* as derived from the structure data (Table I), and

the measured angles were within 1.0 degree of the calculated angles.

In the case of the pattern Figure 8c (insert), one can observe weak

spots between the strong spots (which are indexed in Figure 8d). These

additional weak spots give some hint to the possibility of a super-lattice

occurring in the hydrohausmannite since the weak spots otherwise do not

fit the regular hydrohausmannite structure. On the other hand, the ideal

fitting of the d-value ratios from the strong spots and the good fit of

the angles gave strong evidence for the correctness of the solution.

It is not possible to be quantitative about the relative amounts of

the minerals identified in Table III. In other words, the result of this

table may be related not to the relative abundance but to the more crystal-

line nature of some phases. In addition, only relatively large crystals

(>1/4 μm) produced spot patterns. It was not possible to obtain diffraction

---

*(with the exception of the hydrohausmannite, 2.5 percent larger than in
Appendix 1)

patterns from most of the particles observed. None the less, the occurrence of six out of nine Na-birnessite patterns probably means it is the most prevalent manganese mineral in these nodular samples.

Further examination by high voltage electron microscopy will, of course, facilitate analysis of the denser particles.

Iron Compounds

A synthetic ferric hydroxide, $Fe(OH)_3$, was prepared by the method of Hrynkiewicz et al. (1970) and not allowed to dry out. Using the same electron microscopic preparation methods as already described, figures such as Figure 9 were obtained, with typical diffraction ring patterns, as shown in Figure 10, consisting of three clearly visible rings. Some dehydration, however, must occur during examination in the vacuum of the microscope. The same rings were observed in many samples of nodule powder DWHD-16, as e.g. shown in Figure 11. Here the rings were more or less sharp, and their d-values were identical to those from the synthetic iron hydroxide: 1. ring 2.5 - 2.6 Å, 2. ring 2.1 - 2.2 Å, 3. ring 1.5 Å. It is reassuring to note that these d-values correspond exactly with the most intense lines from van der Giessen (1966, Table 2), and also with the powder diffractometer X-ray work of ASTM card 22-346 for $Fe(OH)_3$, based on data of Okamoto (1968).[*]

The diffuseness (broadening) of the rings as in Figure 11 indicates that a small particle size crystal is responsible for these rings. From the high resolution bright field image, Figure 11, the size of the tiny primary particles may be taken as 30 - 60 Å. Quite often the single

---

[*]Note, that the relative intensities of the three rings (311), (400) and (440) are not the same in Figures 10 and 11; the 1. ring in Figure 11 is particularly strong.

particles are seen clearly, especially in dark field images such as Figure 12b and c. It is interesting that dark field images taken in different sections of the diffuse rings indeed cause different particles to brighten up, as is expected (the small white spots in the upper left parts of Figure 12b, c).

While most of the material consists of the very small $Fe(OH)_3$ particles, as discussed before, in some areas considerably larger particles of the same kind are found. For example, in Figure 13, crystals 100-450 Å in diameter are seen. The particles are densely agglomerated in clusters in this case. Again, different particles become bright in different arc sections of the rings.

Several attempts were made to obtain spot patterns of $Fe(OH)_3$ rather than the rings so that a lattice structure might be indicated. However, they were unsuccessful, which is not surprising in light of the small particle size. Mössbauer spectra have indicated an average particle size of about 100 Å (Johnson and Glasby, 1969). The present results are in agreement with the above statement, showing moreover that there is obviously a large range of sizes.

In conclusion, it may be observed in the last figures, that the ferric hydroxide is present in practically all portions of the powder material. The much larger manganese mineral crystals seem to be embedded in this general mass of ferric hydroxide and only occasionally do they occur as isolated particles. However, this result may depend on the preparation technique since it is likely that the iron hydroxide particles produced in the ultrasonic treatment may have coated the manganese oxide particles by heterocoagulation.

Only in one case a diffraction pattern of an iron mineral other

than Fe(OH)$_3$ was obtained, namely of γ-Fe$_2$O$_3$, see Table III.

Examination of the prepared samples by scanning electron microscopy and microprobe analysis utilizing the Fe-K$_\alpha$ and Mn-K$_\alpha$ X-ray pictures confirmed that both elements, Mn and Fe are practically present everywhere in the samples.

SUMMARY AND CONCLUSIONS

Transmission electron microscopy methods were utilized for detailed study and identification of individual mineral particles in manganese nodules. In an intensive study of two different manganese nodule samples, ten crystal diffraction spot patterns were identified, six as sodium birnessite and one each of todorokite, s-birnessite, and hydrohausmanite, and γ-Fe$_2$O$_3$. Three diffuse Debye-Scherrer rings (d = 2.5, 2.1, 1.5Å) in both synthetic ferric hydroxide and in the manganese nodules, indicate the ferric hydroxide is the main iron mineral in these samples of manganese nodules. The typical particle size of the observed ferric hydroxide ranges of 30 to 60Å, but in some cases, larger particles 100 to 450Å in diameter were observed in clusters. Submicron manganese particles were generally embedded in a mass of smaller ferric hydroxide particles, but this phenomenon may have resulted from the preparation technique. Considerable montmorillonite exists within these nodule samples, particularly the deep-ocean nodule 2P-51.

ACKNOWLEDGEMENTS

APPENDIX 1

No.	Mineral	ASTM File No. or Reference	Structure
	Manganese Compounds		
1.	Synthetic Birnessite	Giovanoli et.al. (1970b)	hex. a=2.84, c=7.22
2.	Na-Birnessite	Giovanoli et.al. (1970a)	ortho. a=8.54, b=15.39, c=14.26
3.	Mn(II) Manganite	18-802	hex. a=5.82, c=14.62
4.	Todorokite	13-164	ortho. a=9.75, b=2.849, c=9.59
5.	Hydrohausmannite	Frondel (1953)	tet. a=5.79, c=9.49
6.	Pyrolusite	12-716	tet. a=4.42, c=2.87
7.	Ramsdellite	7-222	ortho. a=4.533, b=9.27, c=2.866
8.	η''-MnO$_2$	Gattow and Glemser (1961)	ortho. a=4.364, b=9.283, c=2.841
9.	Cryptomelane	Buser and Graf (1955)	tet. a=9.82, c=2.86
10.	ε-MnO$_2$	Gattow and Glemser (1961)	ortho. a=7.63, b=7.79, c=9.32
11.	Hausmannite	16-154	tet. a=5.76, c=9.44
12.	Woodruffite	16-338	tet. a=8.42, c=9.28
13.	Groutite	12-733	ortho. a=4.56, b=10.70, c=2.85
14.	γ-MnO(OH)	Giovanoli and Levenberger (1969)	ortho. a=4.43, b=10.48, c=2.85
15.	Nsutite	17-510	hex. a=9.65, c=4.43
16.	γ-Mn$_2$O$_3$	18-803	tet. a 5.78, c=9.33
17.	Mn$_5$O$_8$	18-801	mon. a=10.34, b=5.72, c=4.85, β=109.4°
18.	Feitknechtite	18-804	hex. a=3.1, c=4.62
19.	Manganoxide	16-350	ortho. a=5.801, b=6.356, c=9.742
20.	Manjiroite	21-1153	tet. a=9.916, c=2.864
21.	Todorokite	18-1411	ortho. a=9.65, b=10.29, c=2.84
22.	Ramsdellite	11-55	ortho. a=4.518, b=9.269, c=2.86
23.	Cryptomelane	12-706	tet. a=9.84, c=2.87
24.	Pyrochroite	12-696	hex. a=3.315, c=4.720
25.	Mn$_3$O$_4$	13-162	cubic; a=8.42
26.	Mn$_2$O$_3$	10-69	cubic; a=9.411
27.	MnO$_{1.88}$	5-673	tet. a=6.97, c=7.12
28.	MnO$_{1.48}$H$_2$O$_{0.15}$	2-829	tet. a=5.78, c=9.43

29.	$(Na,Mn)_4Mn_{12}O_{28} \cdot 8H_2O$	4-95	hex. a=8.4, c=10.1
30.	Elisabetinskite (Co,Mn) O(OH)	12-647	ortho. a=3.725, b=12.38, c=9.455
31.	Crednerite $CuMnO_2$	14-623	mon. a=5.53°, b=2.884, c=5.898, β=104.6°
32.	$Fe_7Mg\ MnO_5(OH)_2$	15-125	hex. a=6.931, c=14.55
33.	Ramsdellite	Giovanoli et.al (1967)	ortho. a=4.44, b=9.351, c=2.849

Iron Compounds

34.	$Fe(OH)_3$	22-346	cubic a=8.37
35.	Goethite	17-536	ortho. a=4.596, b=9.957, c=3.021
36.	$\delta\text{-}FeO(OH)$	13-87	hex. a=2.941, c=4.49
37.	Green rust	13-92	hex. a=3.17, c=10.9
38.	$\beta\text{-}FeO(OH)$	13-157	tet. a=10.48, c=3.023
39.	$\delta\text{-}Fe_{.67}Mn_{.33}O(OH)$	14-557	hex. a=2.905, c=4.555
40.	$\delta\text{-}Fe_{.67}Co_{.33}O(OH)$	14-558	hex. a=2.97, c=4.565
41.	FeO(OH)	18-639	ortho. a=10.70, b=9.80, c=2.964
42.	Ferritin core	22-353	hex. a=11.79, c=9.90
43.	CoFe(III) oxide $CoO\ Fe_2O_3$	3-864	cubic; a=8.33
44.	Hematite	13-534	hex. a=5.032, c=13.737
45.	Magnetite	11-614	cubic a=8.3963
46.	$\gamma\text{-}Fe_2O_3$	15-615	tet. a=8.33, c=24.99
47.	$\gamma\text{-}Fe_2O_2 \cdot H_2O$	8-98	ortho. a=3.88, b=12.54, c=3.07
48.	$\delta\text{-}FeO(OH)$	13-518	hex. a=2.941, c=4.49
49.	Bixbyite $(Mn,Fe)_2O_3$	8-10	cubic; a=9.384
50.	Co_2Fe_3	1-1121	cubic; a=8.39
51.	$MnFe_2O_4$	10-319	cubic; a=8.499

Nickel Compounds

52.	NiO	4-835	cubic; a=4.1769
53.	$\beta\text{-}NiO(OH)$	6-141	hex. a=2.81, c=4.84
54.	$Ni_3O_2(OH)_4$	6-144	hex. a=3.04, c=14.6
55.	$\gamma NiO(OH)$	6-75	hex. a=2.82, c=20.65
56.	$4\ Ni(OH)_2 \cdot NiO(OH)$	6-44	hex. a=3.07, c=23.2
57.	Nickel(III) oxide	14-481	hex. a=4.61, c=5.61
58.	$Ni_2O_2(OH)_4$	13-229	ortho. a=4.81, b=3.00, c=4.65
59.	$Ni(OH)_2$	14-117	hex. a=3.126, c=4.605

60. $NiO \cdot Mn_2O_3$ 1-1110   cubic; a=8.41

61. $NiMnO_3$ 12-269   hex. a=4.905, c=13.59

Copper Compounds

62. $NiO \cdot CuO$ 6-720   tet. a=4.121, c=4.355

63. CuO 5-661   mon. a=4.684, b=3.425, c=5.129, β=99.28

64. Cu_2O 5-667   cubic; a=4.2696

65. $Cu(OH)_2$ 13-420   ortho. a=2.949, b=10.59, c=5.256

66. $Cu(II,I)$ oxide   3-879   tet. a=5.83, c=9.88

Cobalt Compounds

67. Co_2O_3 2-770   hex. a=4.64, c=5.75

68. Co_2O_4 9-418   cubic; a=8.084

69. $Co(OH)_2$ 3-913   hex. a=3.179, c=4.649

70. $\beta-Co(OH)_2$ 2-1094   hex. a=3.19, c=4.66

71. $Co(OH)_2$ 7-169   hex. a=2.855, c=13.156

72. CoO 9-402   cubic; a=4.260

Silicon Compounds

73. Phillipsite   Wenk (1973)   mon. a=10.02, b=14.28, c=8.64, β=125°40'

74. Montmorillonite   12-204   mon. a=5.17, b=9.01, c=13.0, β≈90°?

APPENDIX 2

List of 7 diffraction spot patterns, which could not be solved in agreement with the structures from Appendix A.1.

The given two d-values and the angle define the pattern, compare the explanation to Table II – Accuracy is ±1% for d values and ±1° for angles.

1. d-value	2. d-value	angle
4.46	2.61	90°
3.77	3.39	75°
4.25	3.34	68°
2.83	1.80	95°
7.18	3.83	88°
8.22	7.24	75°
8.03	6.42	94°

REFERENCES

Andryushchenko, P. F., Skornyakova, N. S., 1969. The textures and mineral composition of iron-manganese concretions from the southern part of the Pacific Ocean. Oceanology, 9: 229-42.

Arrhenius, G., 1963. Peragic sediments. In: M. N. Hill (Editor), "The Sea. 3". Interscience, New York, pp. 665-727.

Arrhenius, G. O. S., Bonatti, E., 1965. Neptunism and vulcanism in the ocean. In: M. Sears (Editor), Progress in Oceanography. Pergamon, New York, 3: 7.

Bricker, P. P., 1965. Some stability relations in the system $Mn-O_2$ H_2O at 25° and one atmosphere total pressure. Am. Miner. 50: 1296-354.

Brown, B. A., 1971. A geochemical investigation of inter-element relations in deep-sea ferromanganese nodules. D. Phil. Thesis, University of Oxford.

Burns, R. G., 1965. Formation of cobalt (III) in the amorphous FeOOH· n H_2O phase of manganese nodules. Nature, 205: 999.

Burns, R. G., 1960. Mineralogical Applications of Crystal Field Theory, Cambridge, p. 168.

Burns, R. G., Fuerstenau, D. W., 1966. Electron-probe determinations of inter-element relationships in manganese nodules. Am. Miner., 51: 895-902.

Buser, W., Grütter, A., 1956. Über die Natur der manganknollen. Schweiz. Miner. petrogr. Mitt., 36: 49-62.

Buser, W., Graf, P., 1955. Differezierung von mangan (II) – manganit und $\delta-MnO_2$ durch oberflachenmessung nach Brunauer-Emmet-Teller. Helv. Chim. Acta, 38: 830-4.

Buser, W., Graf, P., Feitnecht, W., 1954. Beitrag zur kenntnis der mangan (II) – manganite und des $\delta-MnO_2$. Helv. Chim. Acta, 37: 2322-33.

Cronan, D. S., 1967. The geochemistry of some manganese nodules and associated pelagic sediments. Ph.D. thesis, University of London.

Frondel, C., 1953. New manganese oxides: Hydrohausmannite and Woodruffite. Am. Min., 38: 761-769.

Fuerstenau, D. W., Herring, A. P., and Hoover, M., 1973. Characterization and Extraction of Metals from Sea Floor Manganese Nodules. A.I.M.E. Trans., 254: 205-211.

Gattow, G., Glemser, O., 1961. Darstellung und eigenschaften von braunsteinen. III. Zeitschrift anorg. allg. Chemie, 309: 9-149.

Giovanoli, R., et al., 1973. Investigation of manganese nodules. Univ. Bern. Inst. anor. Report No. 33a: 1-9.

Giovanoli, R., et al., 1971. Über oxidhydroxide des vierwertigen mangans mit schichtengitter. 3. Helv. Chim. Acta, 54: 1112-1124.

Giovanoli, R., et al., 1970a. Über oxidhydroxide des vierwertigen mangans mit schichtengitter 1. Helv. Chim. Acta, 53: 209-220.

Giovanoli, R., et al., 1970b. Über oxidhydroxide des vierwertigen mangans mit schichtengitter 2. Helv. Chim. Acta, 53: 453-456.

Giovanoli, R., 1969. A simplified scheme for polymorphism in the manganese dioxides. Chimia, 23: 470-472.

Giovanoli, R., Leuenberger, U., 1969. Über die oxydation van manganoxid-hydroid. Helv. Chim. Acta, 52: 2333-2347.

Giovanoli, R., et al., 1968. Ueber ein-und zweiphasige reduktion von γ-MnO$_2$ durch zimtalkohol, Helv. Chim. Acta 51: 355-366.

Giovanoli, R., et al., 1967. Zur struktur des -MnO$_2$. Helv. Chim. Acta 50: 1072-1081.

Glasby, G. P., Hubred, G. L., 1973. Selected bibliography of marine manganese nodules: addendum 2. In preparation.

Glasby, G. P., 1972. Selected bibliography of marine manganese nodules: addendum 1. D. R. Horn (Editor), Ferromanganese Deposits on The Ocean Floor. Columbia University, Palisades, New York, 293 p.

Glemser, O., et al., 1961. Darstellung und eigenschaften von braunsteinen. I. Zeit. Inorg. allg. Chemie, 309: 1-19.

Goldberg, E. D., 1954. Chemical Scavengers of the Sea. Marine Geochemistry. I., 62: 249.

Han, K. N., 1971. Geochemistry and extraction of metals from ocean floor manganese nodules. Ph.D. thesis, University of California, Berkeley, 212 pp.

von Heimendahl, M., 1970. Einführung in die Elektronenmikroskopie. Vieweg-Verlag, Braunschweig, 199 pp.

Hirsch, P. B., et al., 1965. Electron Microscopy of Thin Crystals. Butterworth, London, 549 pp.

Hrynkiewicz, A. Z., et al., 1970. The Mössbauer effect in the Pacific Ocean Fe-Mn nodules. Phy. Stat. Sol. (a), 3: 1039-1045.

Hubred, G. L., 1973. Ph.D. thesis, University of California, Berkeley.

Johnson, C. E., Glasby, G. P., 1969. Mössbauer effect determination of particle size in microcrystalline iron-manganese nodules. Nature, London, 222: 376-7.

Krauskopf, K. B., 1956. Factors controlling the concentrations of thirteen rare metals in sea water. Geochim et Cosmochim. Acta, 9: 1.

McMurdie, H. F., 1944. Microscopic and Diffraction Studies on Dry Cells and their Raw Materials. Trans. Electrochem. Soc., 36: 313.

Mero, J. L., 1965. The Mineral Resources of the Sea. Elsevier, Amsterdam, 312 pp.

Murray, D. J., Healy, T. W., Fuerstenau, D. W., 1968. The adsorption of aqueous metal on colloidal hydrous manganese oxide. Adv. Chem. Series, No. 79: 74.

Okada, A., Shima, M., 1969. Study on the manganese nodule (II) - Comparison of a manganese nodule collected from the surface of the sea-floor with that collected from a 3-metre deep core. J. Japan Ass. Miner. Petrol. econ. Geol., 61: 41-9 (In Japanese).

Okamoto, S., 1968. Structure of the New -Fe_2O_3 (hydrate). J. Am. Chem. Soc., 51: 54.

Stevenson, J. S., Stevenson, L. S., 1970. Manganese nodules from the Challenger Expedition at Redparth Museum. Minerologist, 10: 599-615.

Straczek, J. A., et al., 1960. Studies of the manganese oxides. IV. Todorokite. Am. Miner., 45: 1174-84.

Thomas, G., 1962. Transmission Electron Microscopy of Metals. Wiley, Inc., New York, 299 pp.

Tooms, J. S., et al., 1969. Geochemistry of marine phosphate and manganese deposits. Oceanogr. mar. Biol., 7: 49-100.

Van der Giessen, A. A., 1966. The structure of iron (III) oxide hydrate gels. J. Inorg. Necl. Chem., 28: 2155-2159.

Wenk, H., personal communication, 1973. Department of Geology and Geophysics, University of California, Berkeley.

Willis, J. P., Ahrens, L. H., 1962. Some investigations on the composition of manganese nodules with particular reference to certain trace elements. Geochim. et Cosmochim. Acta, 26: 751.

Zenkevitch, N., Skornyakova, N. S., 1961. Iron and manganese on the ocean bottom. Priroda, 2: 47-50 (In Russian).

TABLE I.   Main Manganese Oxides Found in Manganese Nodules

Name used in this work	Equivalent or earlier names	Structure	Reference
s-birnessite or synthetic birnessite (Mn III manganite IV) ($Mn_7O_{13} \cdot 5\ H_2O$)	δ-MnO_2 7 Å manganite	hexagonal a=2.84,c=7.22	Giovanoli et.al. (1970)b ASTM[*]
Sodium birnessite ($Na_4Mn_{14}O_{27} \cdot 9H_2O$)	7 Å manganite	orthorhombic a=8.54,b=15.39 c=14.26	Giovanoli et.al. (1970)a ASTM[*]
Manganous manganite (Mn II manganite IV) ($4MnO_2, Mn(OH)_2 \cdot 2H_2O$)	birnessite δ-MnO_2 (1965)	hexagonal a=5.82,c=14.62	Buser et.al. (1954) Bricker, ASTM 18-802 (1965)
Todorokite ($MeMn_6O_{12} \cdot 3H_2O$)	"Buserite" 10Å manganite	orthorhombic a=9.75,b=2.849 c=9.59	Straczek et.al. (1960) ASTM 13-164

[*]Proposed structures submitted to ASTM.

TABLE II. Description of the two nodule
samples used in this investigation.

Nodule	Depth (meters)	Longitude	Latidude	Analysis (weight, percent)				
				Mn	Fe	Co	Ni	Cu
2P-51	4900	145°56'W.	9°52'S.	16.8	12.5	0.2	0.6	0.4
DWHD-16	1270	145°33'W.	16°29'S.	24.5	11.5	1.15	0.7	0.25

TABLE III. Solved Diffraction Patterns

Structure	Observed	Fig.	Obs. 1. and 2. d-value		Angle
Na-birnessite	6 times	4	3.74 (2$\bar{2}$0)	1.96 (117)	82°
	(all in	5	2.79 (30$\bar{1}$)	2.245(244)	68°
	DWHD-16)	6	2.60 (312)	2.261($\bar{2}$25)	98°
		-	7.33 ($\bar{1}$01)	3.18 (133)	89°
		-	2.485(3$\bar{2}$2)	1.853($\bar{1}$37)	90°
		-	2.27 (3$\bar{4}$0)	2.23 (244)	86°
s-birnessite	once DWHD-16	7	2.48 (100)	1.43 (110)	30°
Todorokite	once DWHD-16	-	2.65 (302)	2.37 ($\bar{1}$12)	85°
Hydrohausmannite	once 2P-51	8	3.19 (112)	2.97 (200)	58°
γ-Fe$_2$O$_3$	once 2P-51		2.79 (009)	1.96 (331)	85°

FIGURE CAPTIONS

Figure 1.   Typical appearance of nodule powder 2P-51. The number 2
             designates a type 2 particle.

Figure 2.   Typical appearance of nodule powder DWHD-16. The numbers 3
             and 4 designate type 3 and type 4 particles.

Figure 3.   Diffraction pattern of montmorillonite (clay). Practically
             all the flakelike clay settled down parallel to the supporting
             carbon film and resulted therefore always in the same dif-
             fraction pattern as this one. The weak rings through the
             spots are probably produced by tiny fragments of the same
             mineral.

Figure 4.   Crystal in nodule powder DWHD-16 showing "rafted" fine struc-
             ture (compare Giovanoli (1970)). Diffraction pattern identical
             with Na-birnessite. 650 kV, 18000x. Dark field image 4b
             taken in the strongest reflection of the diffraction pattern
             4c close to the primary beam.

Figure 5.   Crystal (circle) typical of the many small particles "type 3"
             in Figure 2 from nodule powder DWHD-16. Diffraction pattern
             identical with Na-birnessite (Table I). 20000x, 100kV.

Figure 6.   Crystal in nodule powder DWHD-16. Diffraction pattern identical
             with Na-birnessite. 650 kV, 18000x.

Figure 7.   Crystal (middle of image) in nodule powder DWHD-16. Diffraction
             pattern identical with s-birnessite (Table I). 20000x, 100 kV.
             The thin crystal is with its hexagonal basal plane parallel to
             the supporting c-films.

Figure 8.   Crystal in nodule powder 2P-51 identified as hydrohausmannite
             (Table I). Bright field image Figure 8a (20000x), 100kV.
             Dark field image 8b was taken with (112), dark field image
             8c with ($\bar{1}$12) reflection. Figure 8d: Schematic diffraction
             pattern magnified from pattern insert in 8c.

Figure 9.   Ferric hydroxide synthetically prepared. 100kV, 20000x.

Figure 10.   Diffraction pattern from area similar as shown in Figure 9.

Figure 11.   High-resolution bright field image of nodule DWHD-16, indi-
             cating the small ferric hydroxide particles of 30-60 Å
             diameter. 650 kV,
             Insert: Diffraction pattern of corresponding area, showing
             the same 3 diffuse rings as synthetic ferric hydroxide.

Figure 12a. Bright field image of ferric hydroxide in nodule DWHD-16,
             producing the same Debye-Scherrer rings as shown in Figure
             11 (inset). 12b and 12c are dark field images taken in

different arc sections of the rings by the same method as in Figure 13. 100 kV, 18000x.

Figure 13. Bright field and corresponding dark-field images of the largest ferric hydroxide particles observed (100-450 Å). In 13b only those particles become bright which diffract into the corresponding arc section of the Debye-Scherrer rings covered by the objective aperture as seen from 13d. (Location of objective aperture indicated by double exposure.) Figure 13c and e correspondingly. 650 kV, 65000x.
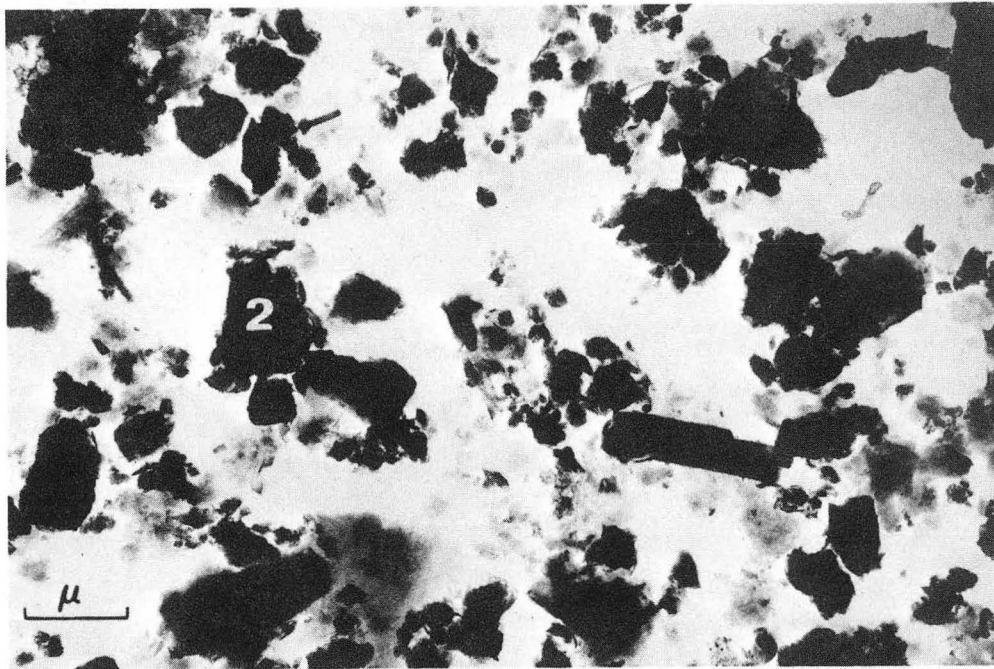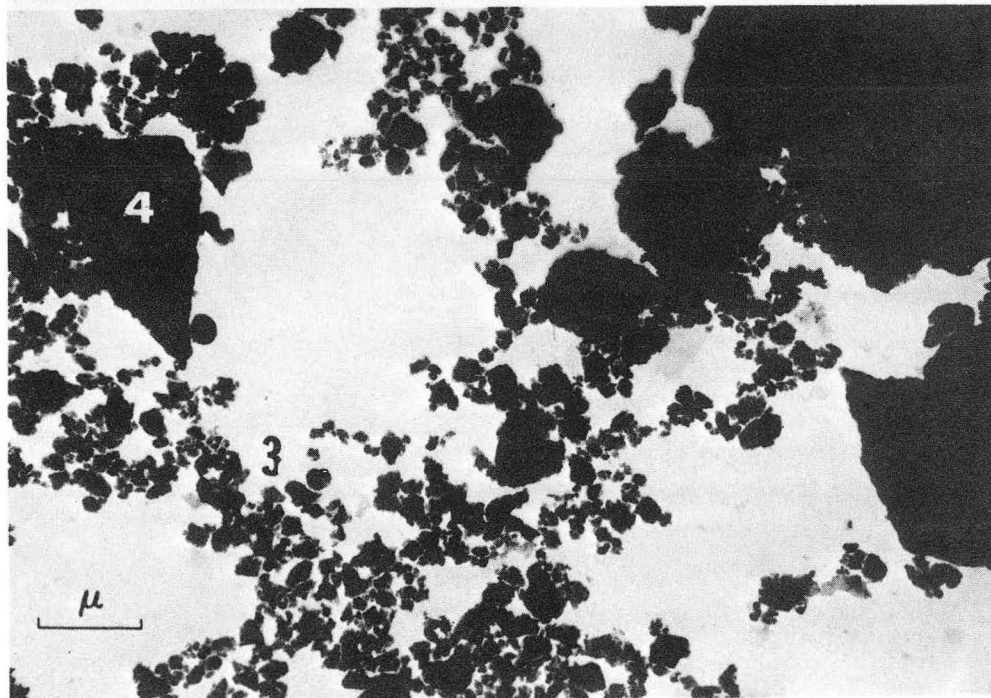
Fig. 1

Fig. 2

XBB 733-2365
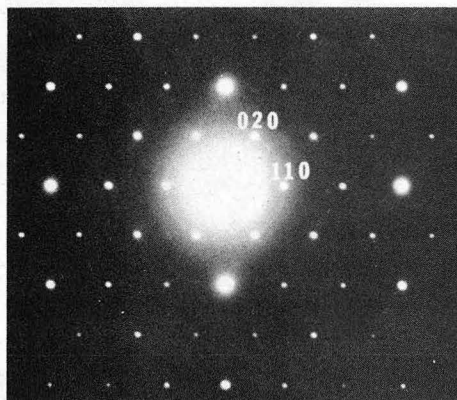
Fig. 3
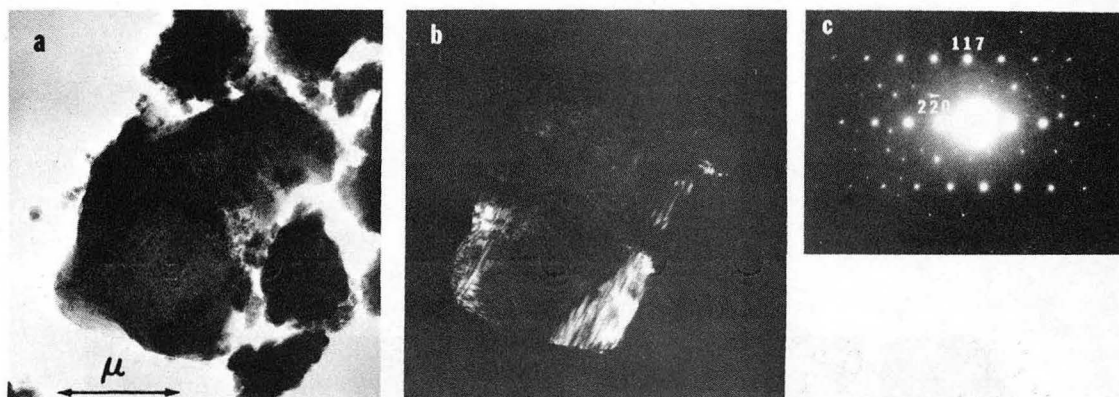
Fig. 4
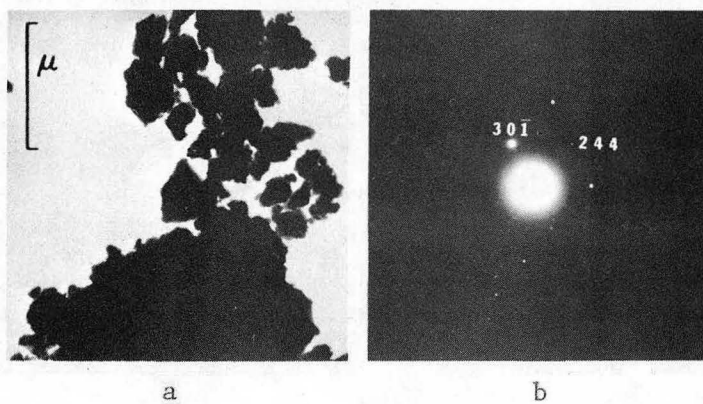
Fig. 5   XBB 733-2364

Fig. 6

a   b
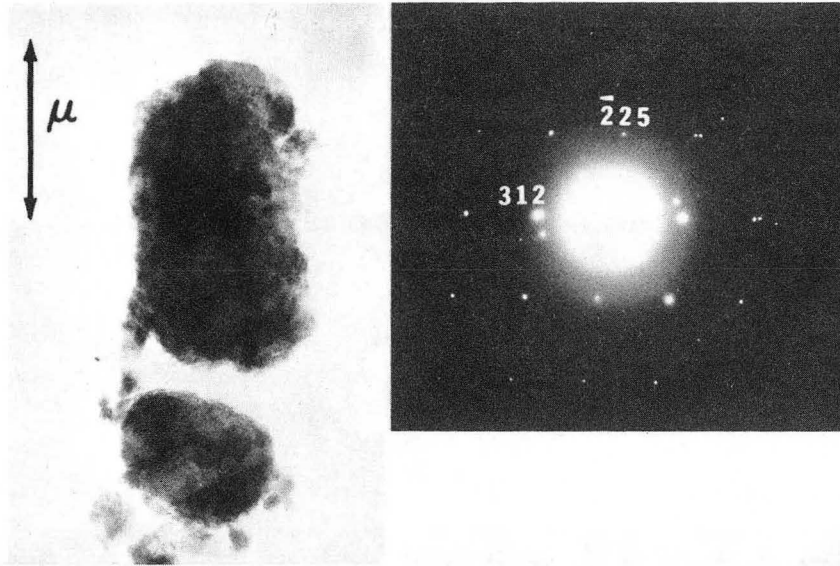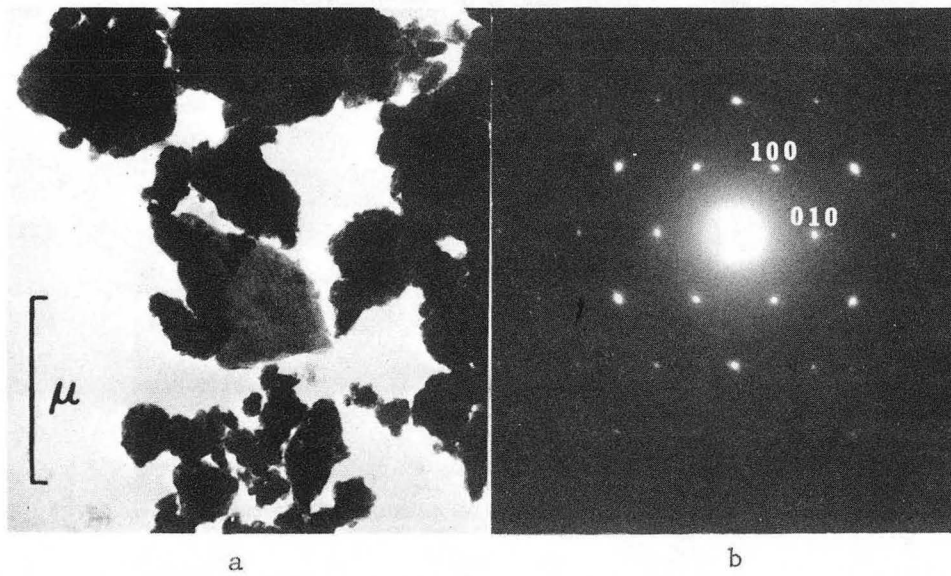
XBB 733-2368

Fig. 7
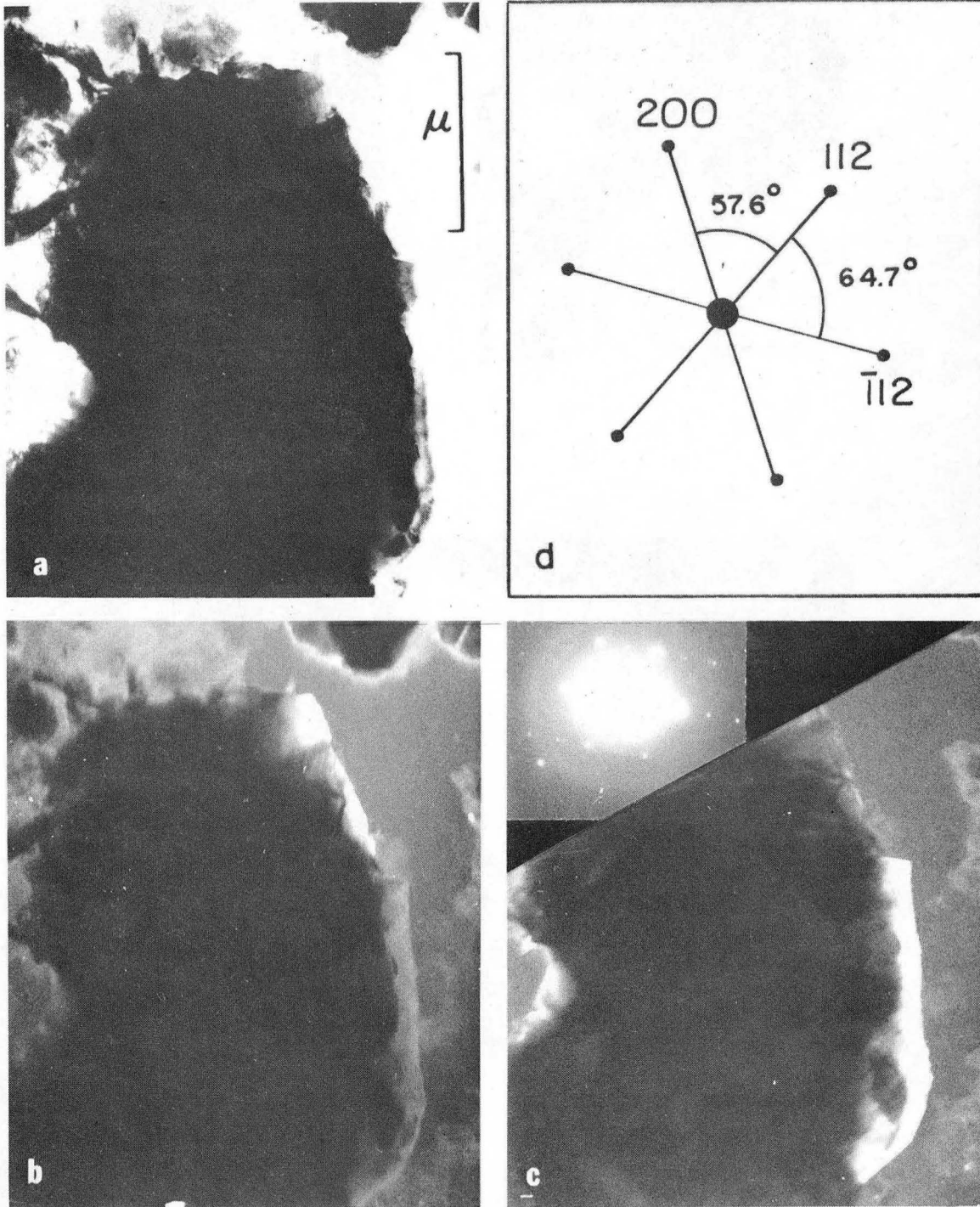
XBB 733-2369

Fig. 8

Fig. 9

Fig. 10

0.1 μ
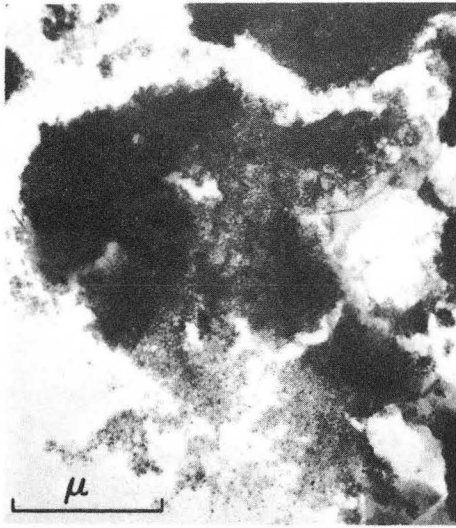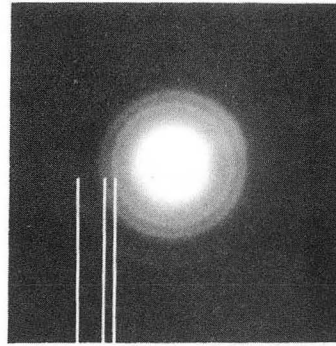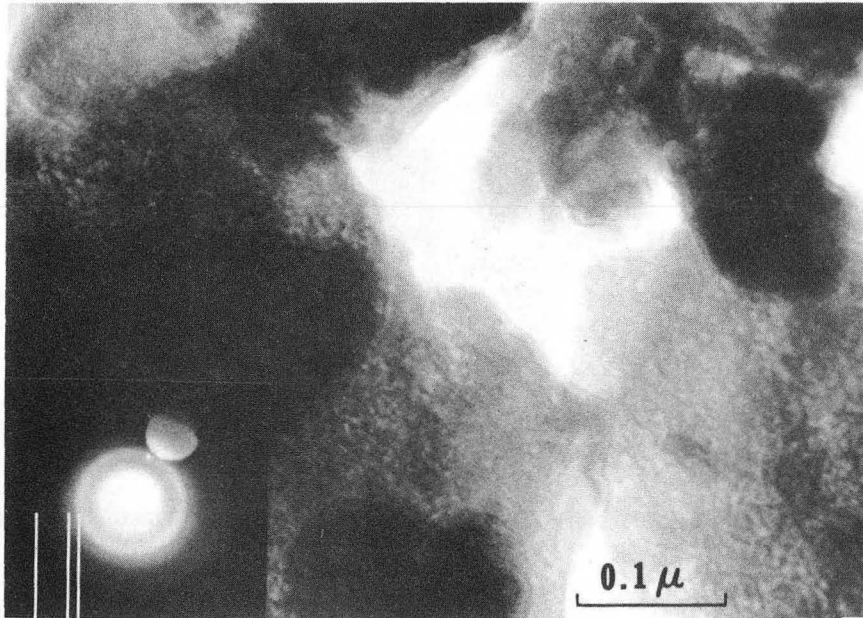
Fig. 11

XBB 733-2366

Fig. 12

XBB 733-2367

Fig. 13